Ocean Engineering 219 (2021) 108385

Contents lists available at ScienceDirect

Ocean Engineering

journal homepage: www.elsevier.com/locate/oceaneng

Simulation study on the hydrodynamic resistance and stability of a disk-shaped autonomous underwater helicopter

Yuan Lin [a], Yue Huang [a], Hai Zhu [a], Haocai Huang [a,b,c,*], Ying Chen [a]

[a] Institute of Ocean Engineering and Technology, Ocean College, Zhejiang University, Zhoushan, 316021, China
[b] Laboratory for Marine Geology, Qingdao National Laboratory for Marine Science and Technology, Qingdao, 266061, China
[c] Key Laboratory of Ocean Observation-Imaging Testbed of Zhejiang Province, Zhejiang University, Zhoushan, 316021, China

ARTICLE INFO

Keywords:
AUV
Computational fluid dynamics
Hydrodynamic instability

ABSTRACT

The hydrodynamic performance during multidirectional motions of a disk-shaped autonomous underwater helicopter, which are being developed recently, are investigated by means of computational fluid dynamics. High mesh quantity is essential to capture the realistic behavior during the horizontal motion. With the saucer-shaped basic geometry, pulsation of the drag force components against and normal to the moving direction is observed during the horizontal motion, which becomes more obvious with increasing velocity, while the motion is hydrodynamically more stable during the vertical movement with a relatively stable zero lateral force. At both moving directions, when the effect of thrusters are considered, the water flux induced by propellers disturbs the flow field, which enhances drag force fluctuation and moving instability. It is concluded that a high-performance controlling system is required to realize a stable and straight motion, or the dishing shape of the vessel needs to be optimized in order to improve the hydrodynamic stability.

1. Introduction

The autonomous underwater vehicles (AUV) are widely used for environmental monitoring in the ocean. The torpedo-shaped AUVs have good straight-line performance due to their streamline profiles (Evans and Nahon, 2004). Therefore, they are suitable for high speed, long-range and quasi-one-directional investigations. Nevertheless, most of the traditional torpedo-shaped AUVs have poor maneuverability (e.g. with large turning diameter) (Tanakitkorn et al., 2017]. Therefore, deploying such AUVs for a small-range work near the seabed with complicated topography is not applicable. By contrast, hovering AUVs can maintain their horizontal and vertical position by numbers of thrusters. As one of such AUVs, the axis-symmetric, disk-shaped, autonomous underwater helicopter (AUH) is being developed in Zhejiang University (Wang et al., 2019] as shown in Fig. 1, which is capable of moving in both horizontal (surge) and vertical (heave) directions in a single posture, and has a zero turning diameter in the horizontal direction. The motions are realized by two vertical thrusters and four horizontal thrusters installed in the hull. Table 1 shows the basic parameters of the AUH of the current version. The cruise of the AUH is mostly achieved by the surge motion, while the AUH has the capability of accurately landing on a certain spot for charging and data exchange by a short-distance heave motion. Therefore, the AUH tends to be used for applications where a greater level of maneuverability is required, e.g. cruise between base stations, close-up inspection et al., near the seabed.

As a common approach, large experimental facilities such as the towing tank, the rotating arm basin are required to capture the detail for the drag force, propulsion, and manoeuvring performance after the vessel model being built. The data are reliable if the test standards is strictly followed, which, however, is a time and money consuming process. Alternatively, the computational fluid dynamics (CFD) is popular in recent years, which has been successfully applied to access the hull resistance and the dynamic stability of the torpedo-shaped AUV (Phillips et al., 2007a,b; Bettle et al., 2009; Phillips et al., 2010; Du et al., 2014; Wu et al., 2014; Salari and Rava, 2017) as well as autonomous underwater gliders (AUG) (Li et al., 2018b, 2019, 2018a). The numerical results has been compared with the experimental data, which shows good reliability (Phillips et al., 2010). While, for AUH, a novel underwater vessel with disk-shaped hull that can move both at its surge and heave directions (as shown in Fig. 1 (b)), the hydrodynamic performance is left to be understood. Recently, computational method has been applied to study the behavior of the AUH, including the route motion stability (Chen et al., 2017), the hydrodynamic interaction when approaches a ship with wave effect (Chen et al., 2019), the water entry

* Corresponding author. Institute of Ocean Engineering and Technology, Ocean College, Zhejiang University, Zhoushan, 316021, China.
E-mail address: hchuang@zju.edu.cn (H. Huang).

https://doi.org/10.1016/j.oceaneng.2020.108385
Received 18 July 2020; Received in revised form 12 November 2020; Accepted 14 November 2020
Available online 24 November 2020
0029-8018/© 2020 Elsevier Ltd. All rights reserved.

Table 1
Basic parameters of the current AUH.

Parameter	Diameter (mm)	Hight (mm)	Weight (kg)	Cruise Speed (m/s)
Value	1557	801	≤ 300	≤ 2

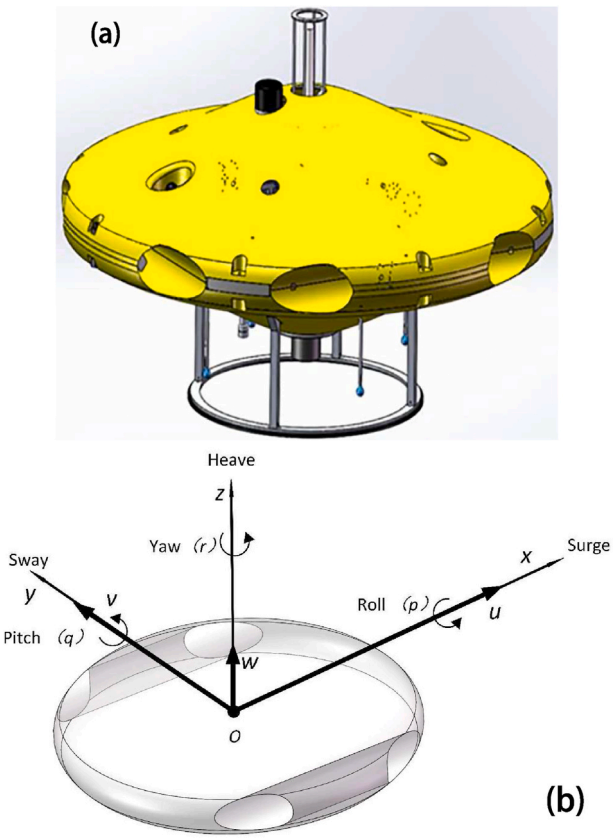

Fig. 1. (a) Diagram of the AUH developed in Zhejiang University; (b) Body-fixed coordinate system for AUH.

impact force (Chen and Lu, 2019), and the Magnus effect (Chen and Jiang, 2019). During the straight line motion, the drag force is mostly considered as a constant at a steady velocity, and it is symmetric about the moving direction. The lateral force normal to the moving direction, and the instant fluctuation has rarely be considered, which, however, may be obvious due to the large length scale at the frontal area at both surge (x-axis) and heave (z-axis) directions, affecting the motion stability. Furthermore, for the AUH developed, the motions in six degrees of freedom (6-DOF) is controlled by two horizontal and two vertical propellers, respectively, which are installed in the through-holes of the hull. This is different from the traditional torpedo-shaped AUV, where the propeller is installed at the stern, i.e. far away from the main hull. Therefore, the hydrodynamic performance of the AUH hull is coupled with hydrodynamic property of the thrusters, which needs to be examined in order to access the practical hydrodynamic performance. In this study, we investigate the hydrodynamic performance of the disk-shaped AUH considering the asymmetry and instability of the flow field, as well as the effect of propellers at both surge and heave motions.

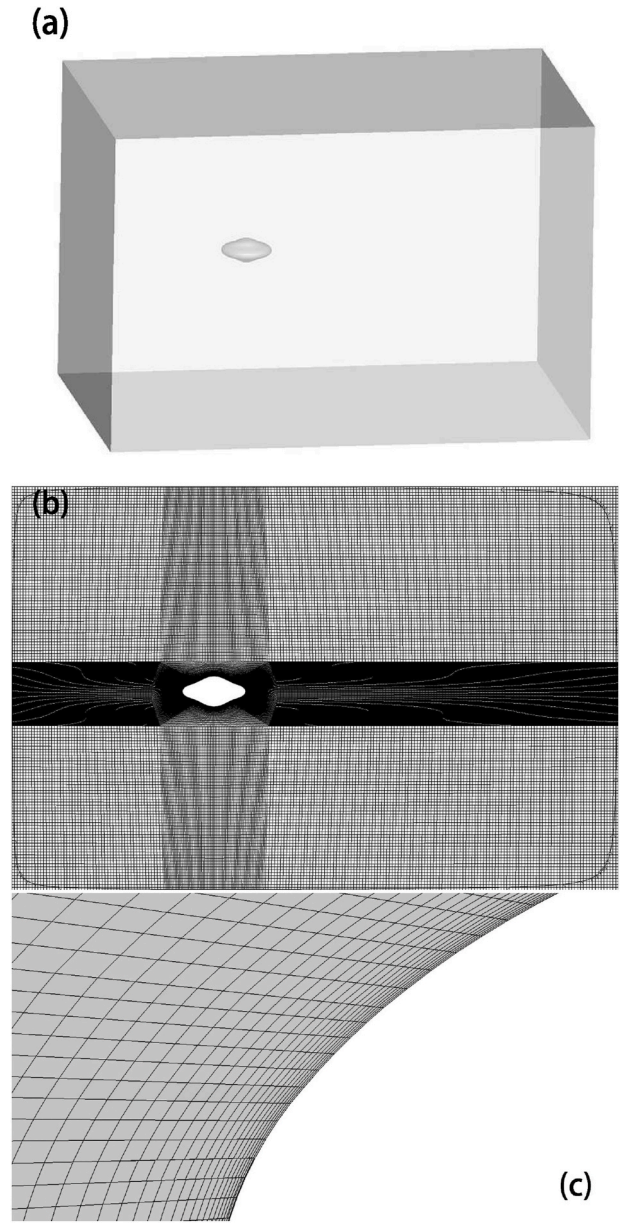

Fig. 2. (a) Simulation domain of the AUH; (b) meshes generated for simulation of the surge motion; (c) refined meshes near the AUH hull. The mesh number is around 11 *million*.

2. Method

As shown by the body-fixed coordinate system for AUH in Fig. 1(b), the surge direction is along the x-axis, and the z-axis is normal to the horizontal (xoy) plane, which is consistent with the vertical (heave) direction. The AUH can take the movement at both surge ($u \neq 0$, $v = w = 0$) and heave ($w \neq 0$, $u = v = 0$) directions. In the simulation, the AUH model is placed in a $10 \times 10 \times 15\ m^3$ cuboid filled with water, as shown in Fig. 2. The center of AUH is $5m$ away from the inflow boundary as well as the side wall, and $10m$ away from the outflow boundary. Both the horizontal (surge) and vertical (heave) motions are studied. The commercial CFD software, ANSYS Fluent, is adopt. The geometry model of the vessel is composed by SOLIDWORKS and then imported to ANSYS

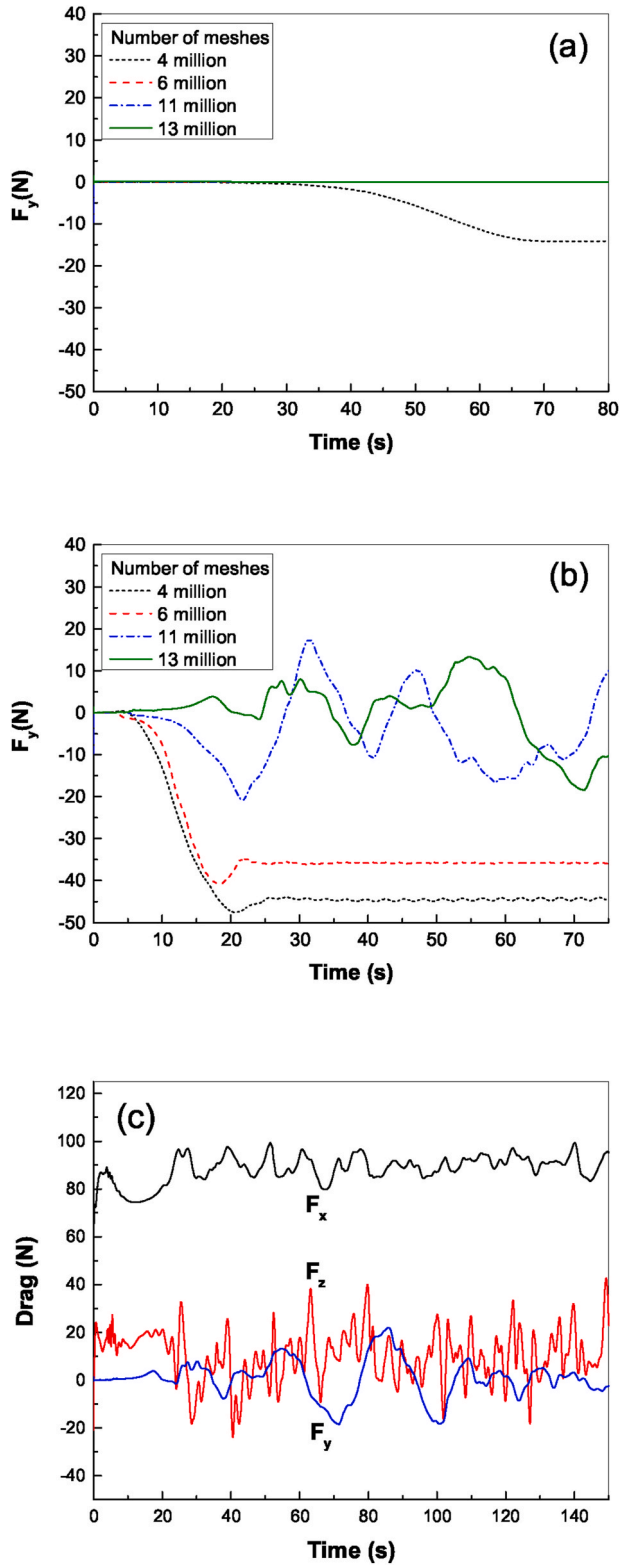

Fig. 3. Change of the lateral force, F_y, during the surge motion at $u = 2\ m/s$ using (a) standard $k-\varepsilon$ model and (b) RNG $k-\varepsilon$ model, respectively, and (c) evolution of the three force components with time at the mesh number of about 13 *million* using the RNG $k-\varepsilon$ turbulence model.

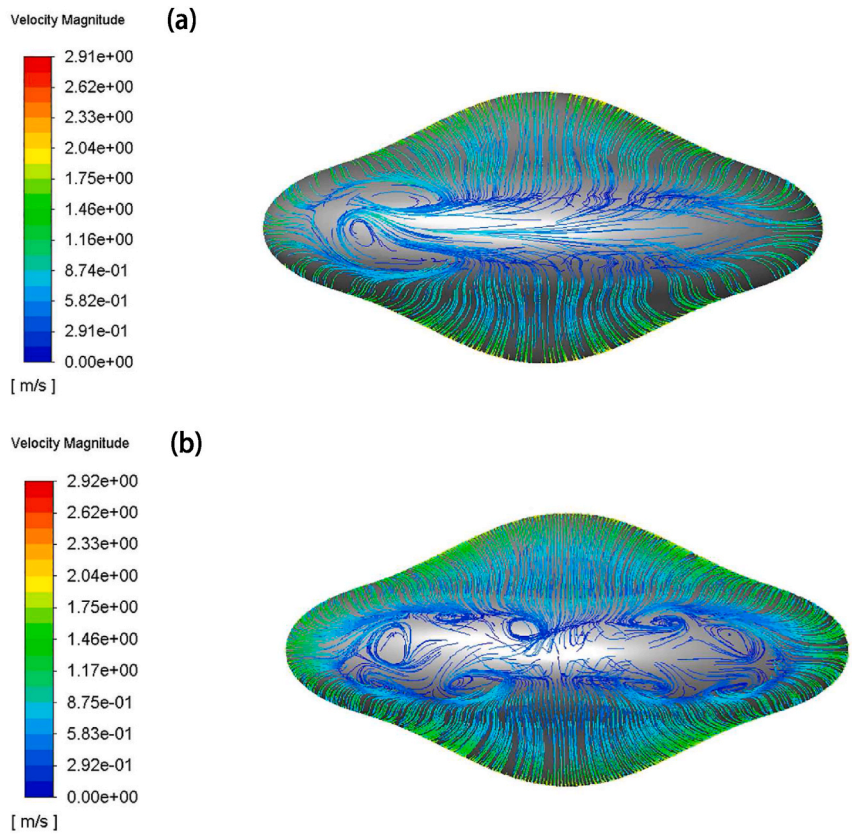

Fig. 4. Stream lines near the surface at the rear of the disk-shaped AUH with (a) 6 *million* meshes and (b) 11 *million* meshes, respectively, during the surge motion at the velocity of 2 m/s.

Table 2
Drag force, F_x, at $u = 2\ m/s$ in simulation based on different number of meshes.

No(s) Meshes	4029664	6251492	11171496	13670746
RNG $k-\varepsilon$	110.18 N	96.73 N	89.10 N	89.66 N
standard $k-\varepsilon$	89.10 N	76.11 N	73.23 N	73.21 N

Table 3
Drag force, F_z, at $v = 1\ m/s$ in simulation based on different number of meshes using RNG $k-\varepsilon$ model.

No(s) Meshes	2281365	3140837	5035164	7341848
Drag Force	592.42 N	554.15 N	516.05 N	524.80 N

ICEM, where structured meshes are generated from the basic geometric model of AUH. In the simulation, the Reynolds Averaged Navier-Stokes (RANS) equations,

$$\frac{\partial \rho}{\partial t} + \frac{\partial}{\partial x_i}(\rho u_i) = 0 \tag{1}$$

and

$$\frac{\partial}{\partial t}(\rho u_i) + \frac{\partial}{\partial x_j}(\rho u_i u_j) = \frac{\partial p}{\partial x_i} + \frac{\partial}{\partial x_j}\left[\mu\left(\frac{\partial u_i}{\partial x_j} + \frac{\partial u_j}{\partial x_i} - \frac{2}{3}\delta_{ij}\frac{\partial u_l}{\partial x_l}\right)\right] + \frac{\partial}{\partial x_j}\left(-\rho\overline{u_i' u_j'}\right) \tag{2}$$

is solved in order to determine the cartesian flow field ($u_i = u, v, w$) and the pressure, p. $u_i = \overline{u}_i + u_i'$, in which $\overline{u}_i$ and u_i' is the mean and fluctuating velocity components. Various turbulence models are developed to provide solutions to the term of Reynolds stresses, $\frac{\partial}{\partial x_j}(-\rho\overline{u_i' u_j'})$, allowing closure of the RANS equations.

The two-equation turbulence model is capable of determining both the turbulent length and the time scale by solving two separate transport equations. As one of such kind, the standard $k-\varepsilon$ model is a popular turbulence model, which is economic and provides satisfying accuracy for a wide range of turbulent-flow problems. This model is based on transport equations for the turbulence kinetic energy, k, and its dissipation rate, ε, in which the model constants have constant values that are determined from experiments for fundamental turbulent flows. The RNG $k-\varepsilon$ model is derived using a statistical technique called renormalization group (RNG) theory. An additional term is included in the ε equation, and the effect of swirling on turbulence is considered, thereby improving the accuracy for swirling flows. Also, an analytical formula is used for determining the turbulent Prandtl numbers instead of a constant value used in the standard model. Furthermore, the RNG $k-\varepsilon$ model is also suitable for low-Reynolds number flows by the inclusion of an analytically-derived differential formula for effective viscosity accounting for low-Reynolds number effects. Therefore, the RNG $k-\varepsilon$ is more precise compared to the standard model. In this study, both the standard $k-\varepsilon$ model and the RNG $k-\varepsilon$ model are used and the results are compared.

In order to model the boundary layer currently, the thickness of the first layer of meshes around the AUH hull is about 1 mm so that $\Delta y^+ \approx 30$, considering that the Reynolds number, $Re = UL/\nu^*$, in the working condition is of $O(10^6)$. U and L are the velocity and the length scale of the vessel, respectively, and ν^* is the kinematic viscosity of the water. The boundary conditions at the wall of the basin, as well as the AUH hull is set to be non-slip. Different time step size from 0.01s to 0.05s is used. Mesh sensitivity is checked in each motion, as will be discussed in detail in the next section.

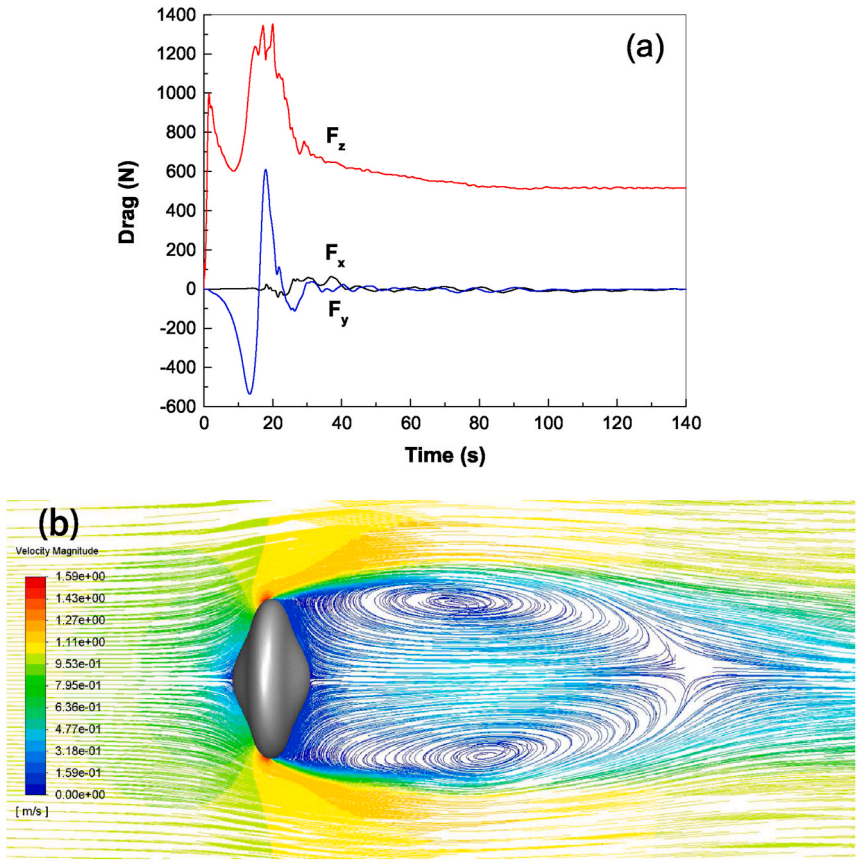

Fig. 5. (a) Time evolution of components of the drag force at x-, y- and z- direction, respectively and (b) Streamlines at the steady state during the heave motion at the velocity of 1 m/s with 5 *million* meshes. The RNG $k-\varepsilon$ model is used.

3. Results and discussion

3.1. Hydrodynamics of the basic geometry

3.1.1. Turbulence model and mesh quantity

The hydrodynamic performance of the basic geometry of AUH is first examined, which is a disk-shaped and axisymmetric geometry as shown in Fig. 4. All the holes and accessories are neglected. The influence of the number of meshes, N, on the simulation result (the mean drag force at the steady state) is examined for both the surge motion and heave motion, with $u = 2\ m/s$ and $w = 1\ m/s$, respectively. The mesh quantity is increased by the refinement of overall surface meshes at the AUH hull.

For the surge motion, as shown in Table .2, it can be found that for both RNG $k-\varepsilon$ and standard $k-\varepsilon$ models, F_x decreases with increasing N, achieving a constant value when N reaches 11 *million*. As shown in Fig. 3, a non-zero and constant lateral force at the sway direction, F_y, can be observed at $N = 4$ *million* using the standard $k-\varepsilon$ model (Fig. 3(a)) The lateral force, F_y becomes zero when N exceeds 6 *million*. Similarly, as can be found in Fig. 3(b), slightly fluctuational F_y is observed using the RNG $k-\varepsilon$ model at low meshes numbers, the average value of F_y at the quasi-steady state is non-zero, which approaches zero when N exceeds 11 *million*, and the calculated force becomes significantly fluctuated. The non-zero lateral force indicates the asymmetry of the flow field at the rear of the vessel, although the geometry is symmetric, as shown by the streamlines in Fig. 4(a), a secondary flow area is observed at the rear left, which causes the non-zero lateral force. The asymmetry is due to the coarse meshes at low N. With finer meshes, the unrealistic asymmetry of the flow field is suppressed. As shown in Fig. 4(b), number of secondary flow area increases, and the flow field becomes nearly symmetric with both xoz plane and xoy plane of the body-fixed coordinate system (Fig. 1 (b)), giving rise to the zero mean of the lateral force. Therefore, the appearance of non-zero F_y is due to the limited resolution of meshes at low N causing the asymmetry of the flow field at the rear. The standard $k-\varepsilon$ is less sensitive to the mesh quantity. However, it can be found that the drag force calculated is significantly smaller than the one based on RNG $k-\varepsilon$ model. The standard $k-\varepsilon$ model underestimates the drag force, which also fails to estimate the fluctuation of the lateral force, therefore, it is not used in the following investigation. For the RNG $k-\varepsilon$ model, a mesh number as high as 10*million* is essential to capture the symmetric flow field around the vessel. In this case, the length scale of the meshes on the surface of the vessel is around 10 *mm*, which is of $O(10^{-3})$ of the AUH length.

For the heave motion, the mesh sensitivity is examined at $w = 1\ m/s$. The change of the drag force, F_z with mesh quantity is shown in Table .3. It can be found that the drag force becomes relatively stable when N exceeds 5 *million*. As shown in Fig. 5(a), a significant fluctuation at the early stage is observed from the drag force curves, which is damped and approaches a steady state after about 100 s. The flow field is nearly symmetric as shown in Fig. 5(b), and the lateral forces, F_x and F_y are zero in average, with relatively small perturbations. Comparing to the magnitude of F_z, the moving stability should not be obviously affected by the hydrodynamic fluctuation, i.e., the heave motion is more stable than the surge motion for the disk shaped AUH. For the time efficient purpose, the meshes quantity is about 5 *million* during the calculation of heave motion in the following.

To summarize, in the following investigation, the RNG $k-\varepsilon$ model is used in order to capture the fluctuation of the flow field at the rear of the vessel. We use 11 *million* and 5 *million* meshes in the simulation of the surge and heave motion, respectively.

3.1.2. Hydrodynamics at different velocities

Change of the mean steady-state drag force as a function of the

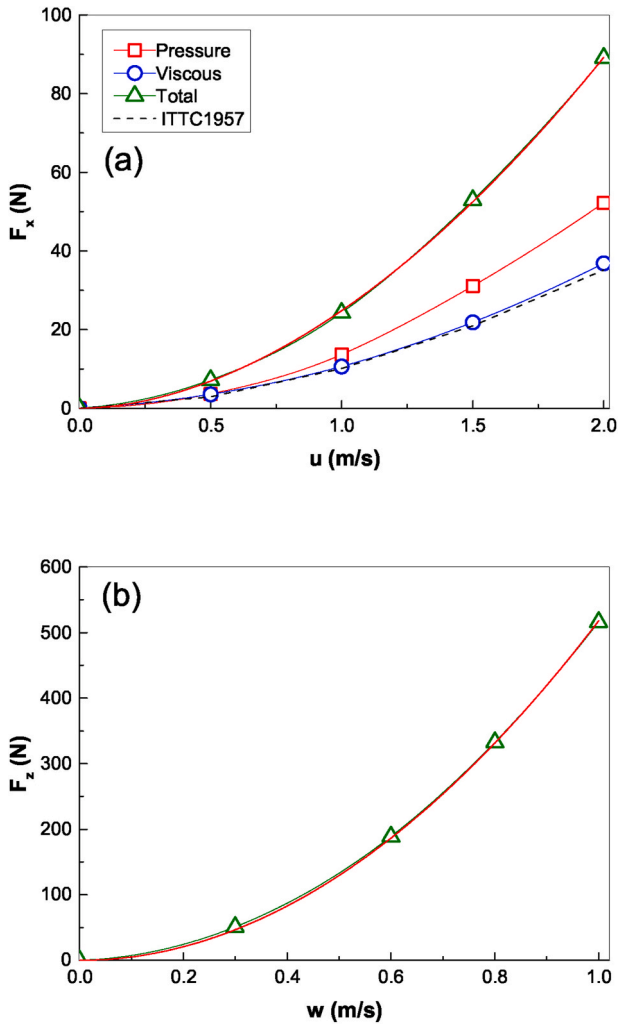

Fig. 6. (a) Drag force as a function of the velocity for AUH during (a) surge and (b) heave motion, respectively. The red solid lines indicate the power-law curve fitting; the black dashed line indicates the curve fitting based on Eq. (1). (For interpretation of the references to colour in this figure legend, the reader is referred to the Web version of this article.)

moving velocity at the surge and heave direction, respectively, is shown in Fig. 6. From the simulation, it can be found that the drag force, F_x and F_z both follow the power law behavior, $F = KU^n$, as shown by the solid red lines in Fig. 6. Here, U is the moving velocity, which is equivalent to u or w during surge or heave motion, respectively. The value of parameters, K and n are listed in Table .4. Obviously, the drag is much larger for heave motion compared to the one for surge motion. The drag force experienced by a submerged vessel is composed of the viscous (friction) drag due to the shear of the fluid flowing along the hull, as well as the pressure (form) drag due to the development and separate of the boundary layer causing the pressure difference along the fore and aft of the hull. At the surge motion, the pressure drag and the viscous drag are comparable in magnitude, as shown in Fig. 6(a). According to the ITTC-1957 (The International Towing Tank Conference 1957) correlation

Table 4
Parameters of for the power-law behavior of the drag force at surge and heave motion, respectively.

Parameter	K	n
F_x	24.83	1.85
F_z	517.98	2

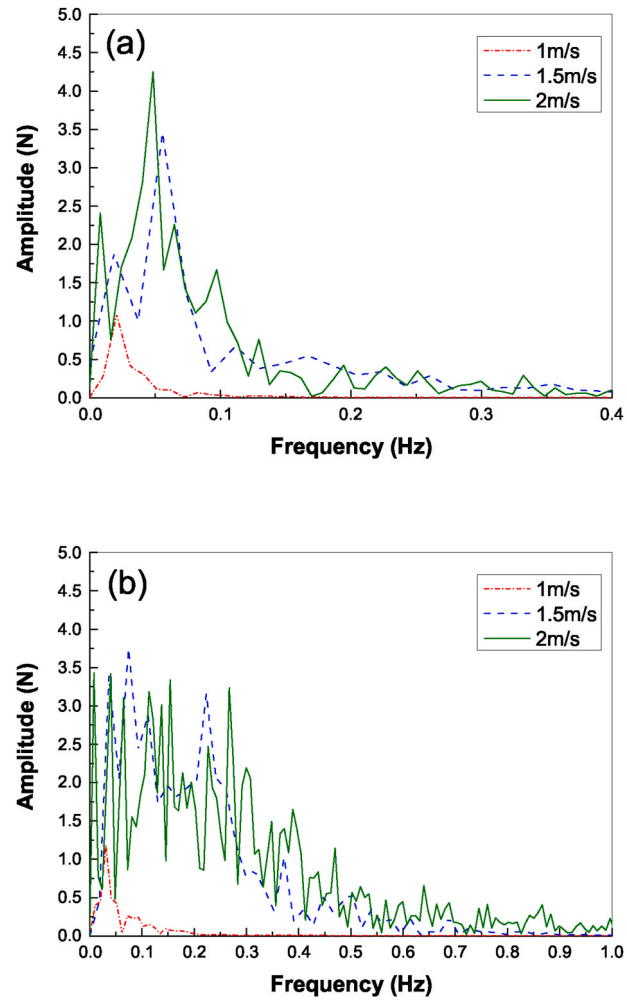

Fig. 7. Analysis at the frequency domain by Fourier Transform for the lateral force of (a) F_y and (b) F_z, respectively, at different surge velocity.

line, the viscous drag coefficient, C_F, is estimated as a function of the Reynolds number, Re,

$$C_F = \frac{0.075}{(log(Re) - 2)^2}, \tag{3}$$

From Fig. 6(a), it can be found that the viscous drag calculated from the simulation fits well the value estimated by Eq. (1). On the other hand, for the heave motion, the viscous drag is negligibly small and not shown in the figure. It seems that the pressure drag approaches a second-order power law behavior with the moving velocity, while the exponent, $n < 2$ for the viscous drag according to Eq. (1), giving rise to $n = 1.85$ calculated for the drag force F_x, during the surge motion.

As mentioned in the previous section, we observe obvious fluctuation of all the drag force components, F_x, F_y and F_z during the surge motion though a steady state is reached, as shown in Fig. 3(c). The fluctuation of

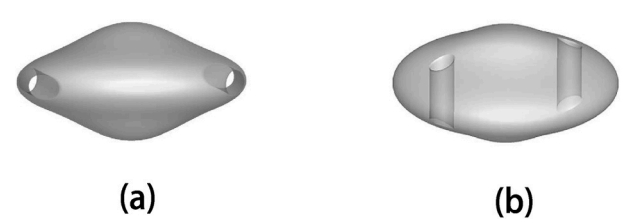

Fig. 8. (a) Geometry model of AUH with (a) horizontal and (b) vertical propellers, respectively, in through holes.

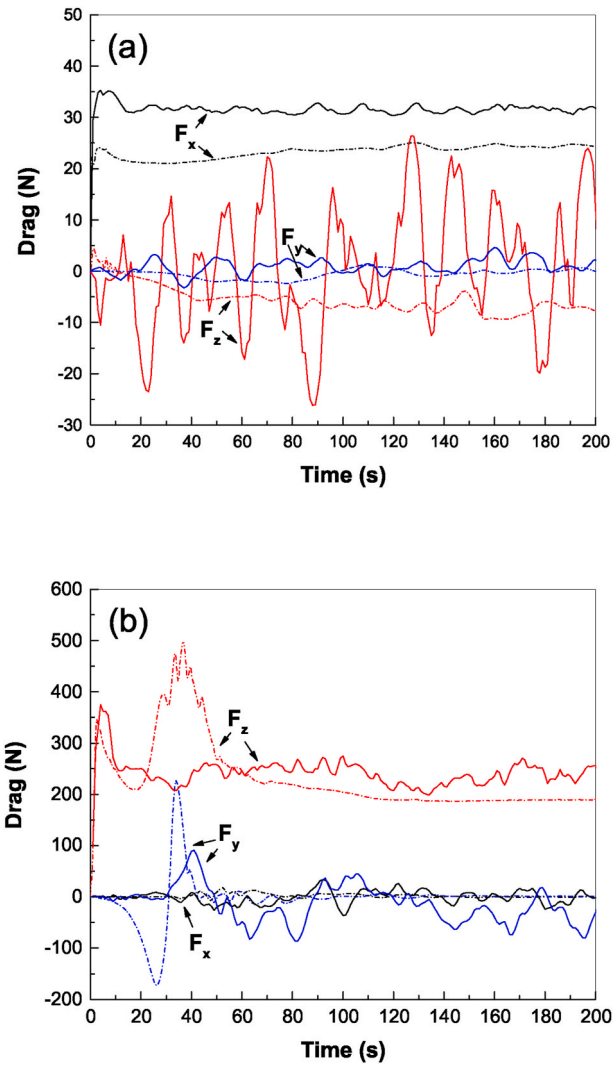

Fig. 9. Time evolution of components of the drag force at x-, y- and z- directions at (a) the surge motion with $u = 1\ m/s$ and (b) the heave motion $w = 0.6\ m/s$, respectively. The solid lines indicates the force calculated using the model with propellers using $\Delta p = 800\ Pa$ for the horizontal propellers (surge motion) and $\Delta p = 5000 Pa$ for the vertical propellers (heave motion), respectively. The dashed lines indicate the force calculated using the basic model.

the lateral force, F_y and F_z, at different velocities is examined at the frequency domain by Fourier transform as shown in Fig. 7. The fluctuation amplitude of F_y and F_z are of the same order, while more high frequency components of the fore signal are found for F_z. This indicates that the fluctuate is more frequently at the vertical direction. Furthermore, the amplitude, as well as the distribution width at the frequency domain increases with increasing u. The fluctuation is greatly reduced when u is decreased to e.g., $1\ m/s$. The existence of the fluctuational drag force would affect the motion stability of the vessel, which prevents the AUH from moving in a straight trajectory and with a stable cruising speed.

3.2. Hydrodynamics with the influence of propellers

The investigation above focuses on the hydrodynamic properties of the basic geometry of AUH. Nevertheless, the propellers will further complicate the hydrodynamic properties of AUH in the working condition, since it is installed close to the main hull, different from the torpedo-shaped AUVs. In order to investigate the effect of thrusters, the basic model of AUH is modified as shown in Fig. 8. The propellers are installed in through holes of the hull with their axis parallel to the surge and heave directions, respectively. The diameter of the through holes is $169\ mm$. We first consider the condition of surge motion with the working of two propellers with their axis arranged along the surge direction (Fig. 8(a)). According to the ideal propeller theory, the propeller is simplified as a round plane located in the middle of through-holes, which produces a controllable local pressure increment, Δp, when the fluid pass through the plane. The tangential force caused by the rotation of the propeller is not considered here, since the two propeller are symmetric with xoz plane. We investigate the situation that the AUH moves at the surge velocity of $1\ m/s$, while the propellers induce a pressure increment of $800\ Pa$ producing the total thrust of $35.9\ N$ considering the propeller plane has a diameter of $169\ mm$. 10476861 structured meshes are generated for the computation. The average drag force at the steady state in the surge direction, $F_x = 31.44\ N$ as is calculated from the simulation. Therefore, a realistic working condition at $u = 1\ m/s$ for the propellers is approached. As shown in Fig. 9(a), F_x is considerably larger than the one calculated from the basic geometry. All the force components become more fluctuated. In particular, F_z becomes significant unstable, giving rise to a pronounced disturbance at the vertical direction on the rear of the vessel during the surge motion. As shown in Fig. 10(a), the enhance of the fluctuation should be due to the disturbance of the previous flow field by the stream from the propellers. This should be given careful attention considering the motion stability.

On the other hand, as shown in Fig. 9(b), influence of two vertical propellers during the heave motion is investigated at $w = 0.6\ m/s$. The pressure difference of the propeller plane is set to be $5000\ Pa$, giving rise to a thrust of $224\ N$. This is close to the vertical drag, F_z, which is about $230\ N$ calculated from the simulation shown in Fig. 9(b). Therefore, the simulation approaches the practical working condition of the vessel at $w = 0.6\ m/s$. 7302897 structured meshes are generated in the calculation. It can be found that F_z also increases compared to the one from the basic geometry. The drag force becomes fluctuated at all three directions with the working of the propellers as similar to the surge motion, while for the three force components, the fluctuation is comparable in magnitude. As shown in Fig. 10(b), the water flux produced by thrusters disturbs remarkably the previous symmetric and stable vortex (shown in Fig. 5(b)), which causes the hydrodynamic fluctuation. Therefore, the heave motion becomes unstable compared to the basic geometry. Such fluctuation may hinder the accurate landing of the vessel on a certain spot for the purpose of charging, data transfer et al., which also needs to be paid attention.

For a qualitative comparison, the previously developed AUH, which has the diameter of $1000\ m$ and the hight of $430\ mm$, as shown in Fig. 11 (a), is used to perform a horizontal linear motion test in a pool [Wang et al.(2019)], in order to check the hydrodynamic stability of the disk-shaped vessel. In the experiment, the AUH is driven by a pair of horizontal propellers to achieve the initially horizontal linear motion with different mean velocities. The vertical propellers are all off in the test. A nine-axis attitude sensor is installed to measure the attitude during the motion. As shown in Fig. 11(b), an obvious pitch vibration can be observed. The fluctuation amplitude increases with increasing velocity. Due to the vibration, the vessel cannot maintain a constant depth in the water. At the velocity of $0.22\ m/s$, the curve stops when the vessel touches the bottom of the pool. In the previous study (Wang et al., 2019), the vibration is considered to be caused by the positioning unit installed at the center of the hull bottom (the cylinder shaped geometry as shown in Fig. 11(a)), which breaks the symmetric geometry of the hull, giving rise to an additional hydrodynamic moment, M_{fp}, along the pitch direction. Meanwhile, the restoring force by the gravity increases with the pitch angle and resists the rotation. According to Wang et al. (2019), the equation describing the pitch motion can be written as

$$-GR_{BG}sin\theta + M_{Fh} + M_{fp} - M_{fq} = J_q\frac{d^2\theta}{dt^2}, \tag{4}$$

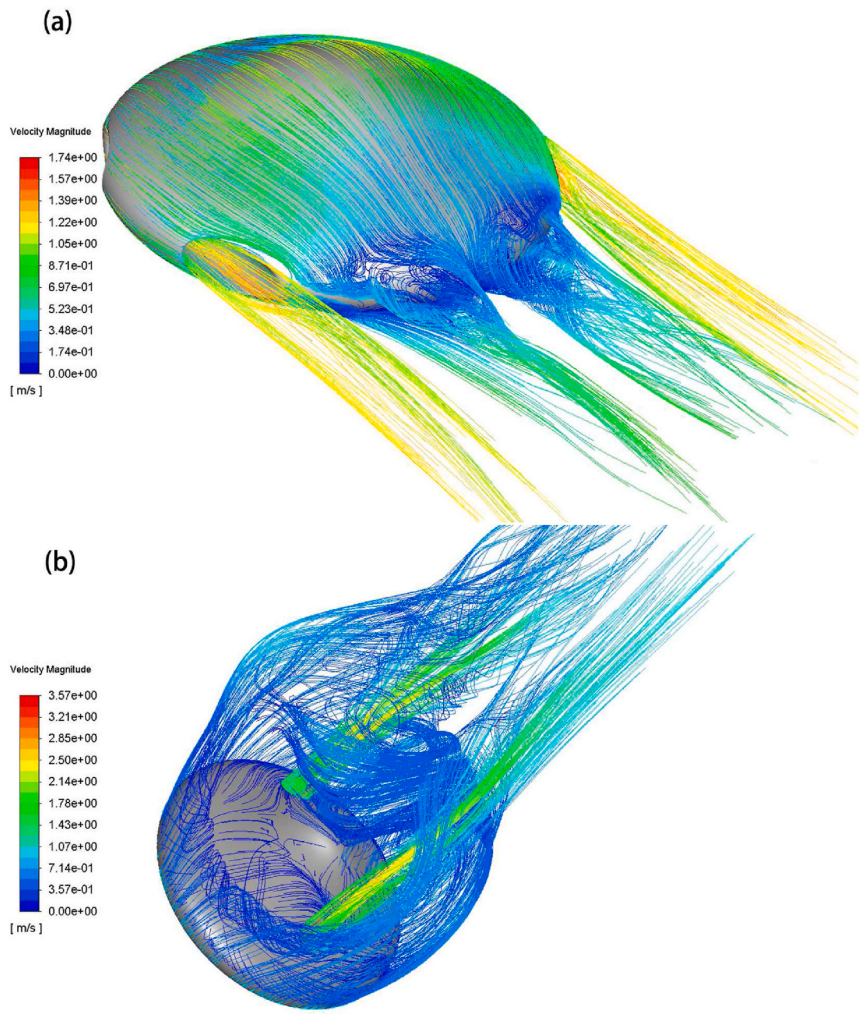

Fig. 10. Stream lines at the steady state for the AUH geometry with (a) two horizontal propellers at the surging velocity of 1 m/s, and (b) two vertical propellers at the heaving velocity of 0.6 m/s, respectively.

where G is the gravity force. R_{BG} is the distance between the center of gravity and the center of buoyancy. θ is the pitch angle. M_{F_h} is the moment by the thrusters. M_{fq} is the moment of hydrodynamic drag against the pitch motion. J_q is the rotating inertia. Eq. (4) may lead to an overdamped or underdamped system, and a stable motion can be achieved at the final stage with a constant pitch angle (Wang et al., 2019). This, however, is not consistent with the result shown in Fig. 11(b), in which it is indicated that the vibration is not damped with time. Therefore, we may deduce that the large fluctuation of the hydrodynamic lateral force, F_z observed in the simulation, should contribute considerably to the pitch vibration behavior. The vibration period is estimated to be 10 to 15 s, insensitive to the moving velocity. The period of the pitch angle from the experiment and F_z from the simulation (see Fig. 9(a)) are of the same order, regardless that the size of the AUH tested is considerably smaller than the current version adopt for simulation, and the surge velocity in the experiment is lower.

From the investigation above, it can be deduced that the novel dish-shaped under water vehicle has an unstable hydrodynamic character. A high-performance closed-loop control system is required in order to realize a straight trajectory with a constant speed at both surge and heave directions. Also, the axis-symmetric shape should be adjusted in order to improve the hydrodynamic stability. For example, an asymmetric fore-aft structure, where the edge at the aft is sharpened, may suppress the secondary flow shown in Fig. 4(b), thereby improve the hydrodynamic stability. The study on the shape optimization will be carried out in the next step.

4. Conclusion

The hydrodynamic performance of the disk-shaped AUH moving at both surge (x-axis) and heave (z-axis) directions are investigated by CFD method. At the surge motion, an unstable state is achieved with the fluctuation of the force components at all three directions. This is due to the fluctuation of the flow field caused by the disk-shaped geometry of the vessel. The fluctuation grows significantly with increasing surging velocity. The working of the two horizontal propellers further enhances the unstable behavior, and cause large fluctuation of the lateral force at the vertical direction. The hydrodynamic instability observed in the simulation agrees with the experimental result, with fluctuation periods being of the same order. During the heave motion, a relatively stable movement can be achieved for the basic disk-shaped geometry, while the stability would also be disturbed by the working of two vertical propellers. A high-performance controlling system is required in order to realize a long-term stable and straight motion at both horizontal and vertical directions. Also, the dishing shape of the vessel needs to be optimized in order to improve the hydrodynamic stability.

CRediT authorship contribution statement

Yuan Lin: Conceptualization, Methodology, Software, Writing -

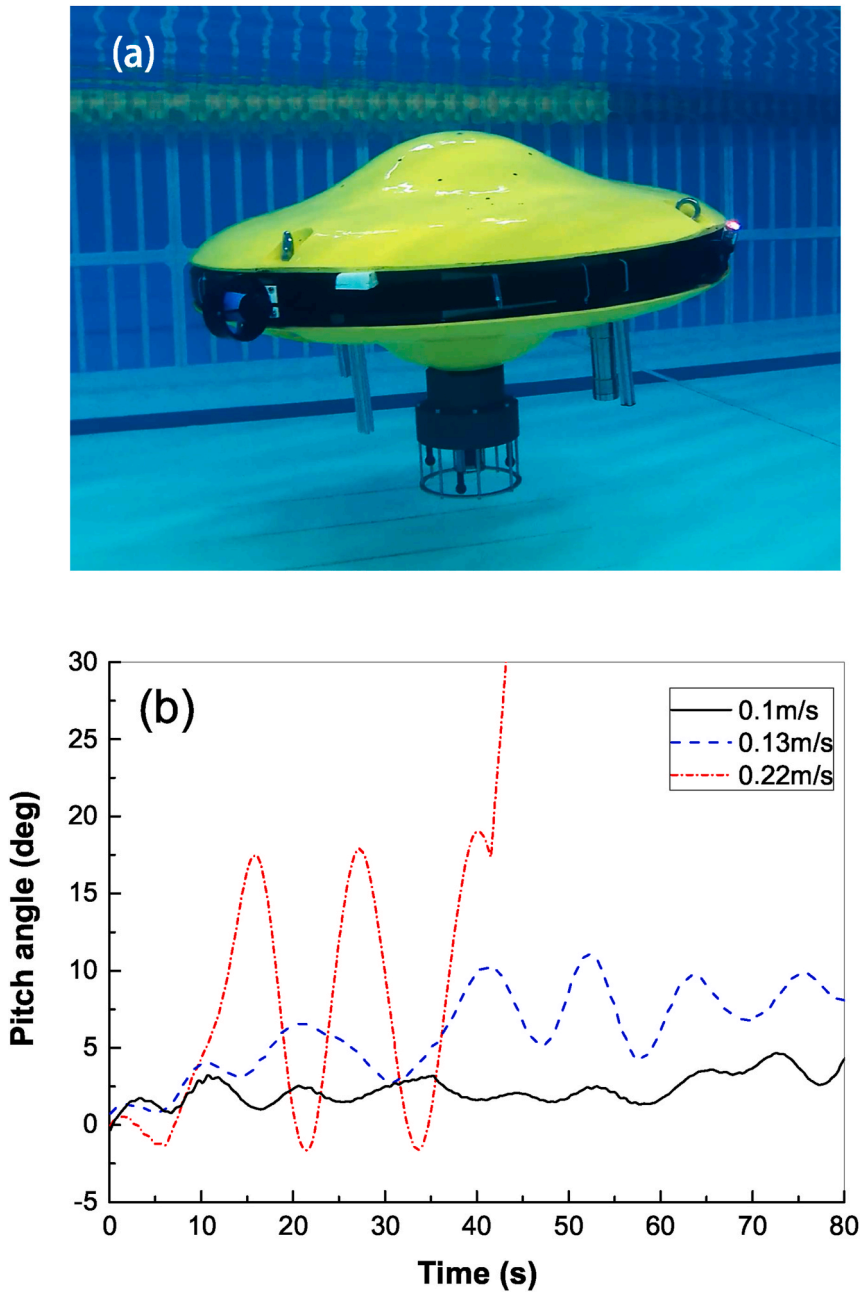

Fig. 11. (a) Experimental test of the AUH developed previously; (b) time evolution of the pith angle during the initially horizontal linear motion.

review & editing, Validation. **Yue Huang:** Data curation, Writing - original draft. **Hai Zhu:** Visualization, Investigation. **Haocai Huang:** Supervision, Investigation. **Ying Chen:** Supervision, Investigation.

Declaration of competing interest

The authors declare that they have no known competing financial interests or personal relationships that could have appeared to influence the work reported in this paper.

Acknowledgments

This study is supported by National Natural Science Foundation of China (41976055), the National Key R & D Program of China (Grant No. 2017YFC0306100)), the Fundamental Research Funds for ZheJiang Provincial Colleges & Universities (No.2019XZZX003-07), and Wenhai Program of QNLM (2017WHZZB0302).

References

Bettle, M.C., Gerber, A.G., Watt, G.D., 2009. Unsteady analysis of the six dof motion of a buoyantly rising submarine. Comput. Fluid 38, 1833–1849.

Chen, C.-W., Chen, Y., Cai, Q.-W., 2019. Hydrodynamic-interaction analysis of an autonomous underwater hovering vehicle and ship with wave effects. Symm. Basel 11, 1213.

Chen, C.-W., Jiang, Y., 2019. Computational fluid dynamics study of magnus force on an axis-symmetric, disk-type auv with symmetric propulsion. Symmetry 11. https://doi.org/10.3390/sym11030397.

Chen, C.-W., Jiang, Y., Huang, H.-C., Ji, D.-X., Sun, G.-Q., Yu, Z., Chen, Y., 2017. Computational fluid dynamics study of the motion stability of an autonomous underwater helicopter. Ocean Eng. 143, 227–239.

Chen, C.-W., Lu, Y.-F., 2019. Computational fluid dynamics study of water entry impact forces of an airborne-launched, axisymmetric, disk-type autonomous underwater hovering vehicle. Symmetry 11. https://doi.org/10.3390/sym11091100.

Du, X., Wang, H., Hao, C., Li, X., 2014. Analysis of hydrodynamic characteristics of unmanned underwater vehicle moving close to the sea bottom. Defence Technol. 10, 76–81.

Evans, J., Nahon, M., 2004. Dynamics modeling and performance evaluation of an autonomous underwater vehicle. Ocean Eng. 31, 1835–1858.

Li, Y., Hu, J., Zhao, Q., Pan, Z., Zheng, M., 2018a. Hydrodynamic performance of autonomous underwater gliders with active twin undulatory wings of different aspect ratios. J. Mar. Sci. Eng. 8, 476.

Li, Y., Pan, D., Ma, Z., Zhao, Q., 2019. Aspect ratio effect of a pair of flapping wings on the propulsion of a bionic autonomous underwater glider. J. Bionic Eng. 16, 145–153.

Li, Y., Pan, D., Zhao, Q., Ma, Z., Wang, X., 2018b. Hydrodynamic performance of an autonomous underwater glider with a pair of bioinspired hydro wings–a numerical investigation. Ocean Eng. 163, 51–57.

Phillips, A., Furlong, M., Turnock, S., 2007a. The use of computational fluid dynamics to determine the dynamic stability of an autonomous underwater vehicle. In: 10th Numerical Towing Tank Symposium (NuTTS'07). Hamburg, Germany.

Phillips, A., Furlong, M., Turnock, S.R., 2007b. The use of computational fluid dynamics to assess the hull resistance of concept autonomous underwater vehicles. In: OCEANS 2007 - Europe.

Phillips, A.B., Turnock, S.R., Furlong, M., 2010. The use of computational fluid dynamics to aid cost-effective hydrodynamic design of autonomous underwater vehicles. Proc. IME M J. Eng. Marit. Environ. 224, 239–254.

Salari, M., Rava, A., 2017. Numerical investigation of hydrodynamic flow over an auv moving in the water-surface vicinity considering the laminar-turbulent transition. J. Mar. Sci. Appl. 16, 298–304.

Tanakitkorn, Wilson, Turnock, PhillipsTanakitkorn, K., Wilson, P.A., Turnock, S.R., Phillips, A.B., 2017. "Depth control for an over-actuated, hover-capable autonomous underwater vehicle with experimental verification. Mechatronics 41, 67–81.

Wang, Z., Liu, X., Huang, H., Chen, Y., 2019. Development of an autonomous underwater helicopter with high maneuverability. Appl. Sci. Basel 9.

Wu, L., Li, Y., Su, S., Yan, P., Qin, Y., 2014. Hydrodynamic analysis of auv underwater docking with a cone-shaped dock under ocean currents. Ocean Eng. 85, 110–126.